01 May 2010

Fringe Visibility Enhanced Extrinsic Fabry-Perot Interferometer using a Graded Index Fiber Collimator

Yinan Zhang

Yanjun Li

Tao Wei

Xinwei Lan

et. al. For a complete list of authors, see https://scholarsmine.mst.edu/civarc_enveng_facwork/566

Recommended Citation

Y. Zhang et al., "Fringe Visibility Enhanced Extrinsic Fabry-Perot Interferometer using a Graded Index Fiber Collimator," *IEEE Photonics Journal*, vol. 2, no. 3, pp. 469-481, Institute of Electrical and Electronics Engineers (IEEE), May 2010.
The definitive version is available at https://doi.org/10.1109/JPHOT.2010.2049833

IEEE Photonics Journal
An IEEE Photonics Society Publication

Fringe Visibility Enhanced Extrinsic Fabry–Perot Interferometer Using a Graded Index Fiber Collimator

Volume 2, Number 3, June 2010

Yinan Zhang
Yanjun Li
Tao Wei
Xinwei Lan
Ying Huang
Genda Chen
Hai Xiao

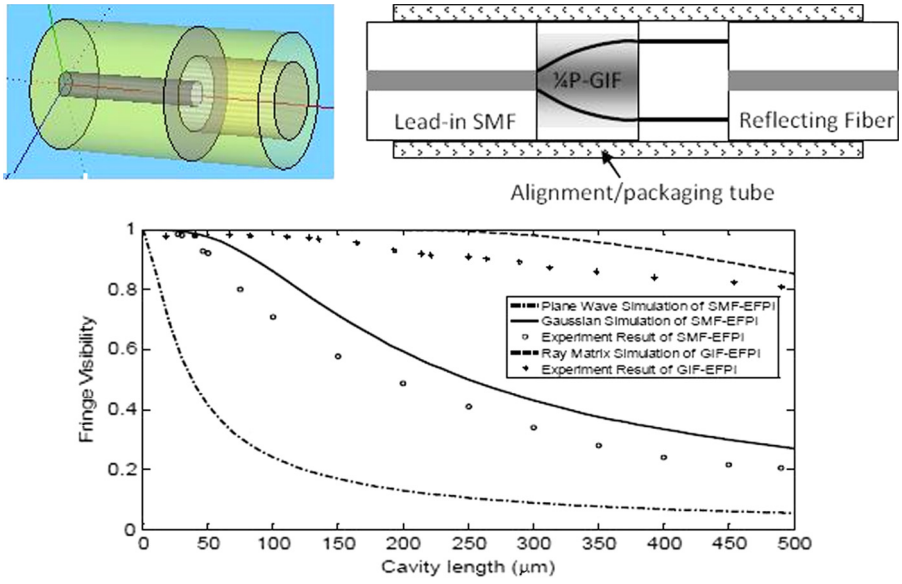

DOI: 10.1109/JPHOT.2010.2049833
1943-0655/$26.00 ©2010 IEEE

Fringe Visibility Enhanced Extrinsic Fabry–Perot Interferometer Using a Graded Index Fiber Collimator

Yinan Zhang,[1] Yanjun Li,[1,2] Tao Wei,[1] Xinwei Lan,[1] Ying Huang,[3] Genda Chen,[3] and Hai Xiao[3]

[1]Electrical and Computer Engineering, Missouri University of Science and Technology, Rolla, MO 65409 USA
[2]College of Electrical Engineering, Henan University of Technology, Zhengzhou City, 450007, China
[3]Civil, Architectural, and Environmental Engineering, Missouri University of Science and Technology, Rolla, MO 65409 USA

DOI: 10.1109/JPHOT.2010.2049833

Manuscript received April 13, 2010; revised April 30, 2010; accepted April 30, 2010. Date of publication May 10, 2010; date of current version June 11, 2010. Corresponding author: H. Xiao (e-mail: xiaoha@mst.edu).

Abstract: We report a fringe visibility-enhanced extrinsic Fabry–Perot interferometer (EFPI) by fusion splicing a quarter-pitch length of a graded-index fiber (GIF) to the lead-in single mode fiber (SMF). The performance of the GIF collimator is theoretically analyzed using a ray matrix model and experimentally verified through beam divergence angle measurements. The fringe visibility of the GIF-collimated EFPI is measured as a function of the cavity length and compared with that of a regular SMF-EFPI. At the cavity length of 500 μm, the fringe visibility of the GIF-EFPI is 0.8, while that of the SMF-EFPI is only 0.2. The visibility-enhanced GIF-EFPI may provide a better signal-to-noise ratio (SNR) for applications where a large dynamic range is desired.

Index Terms: Fabry–Perot interferometers, Optical fiber transducers, Optical fiber device fabrication, Optical fiber interference.

1. Introduction

Optical fiber extrinsic Fabry–Perot interferometers (EFPI) have found many sensing applications in recent years [1]. An EFPI device can be easily made by packaging two cleaved optical fibers into a capillary tube, leaving an air gap between the two fiber endfaces. Reflections of light from the two cleaved fiber surfaces form an interference signal that can be recorded and processed to find the cavity length. When used as a sensor, the optical length (i.e., the product of the cavity length and the refractive index of the medium filling the cavity) changes as a function of the parameters to be measured. With proven advantages such as immunity to electromagnetic interference (EMI), high resolution, small size, and structural ruggedness, EFPI sensors have been demonstrated for measurement of a wide variety of parameters including temperature [2], strain [3], pressure [4], displacement [5], ultrasound [6], magnetic field [7], and refractive index [8].

Using two cleaved optical fibers (typically single mode fibers) to fabricate an EFPI sensor is straightforward and cost effective. However, such a sensor has a fringe visibility decreasing rapidly as cavity length increases due to the divergence (typically about 6–8°, depending on the fiber type) of the beam exiting from the lead-in single mode fiber (SMF). The decreasing fringe visibility could result in a reduced signal-to-noise ratio (SNR), and thus, a limited maximum cavity length for certain applications where a long initial cavity length or large dynamic range is required, for example, for

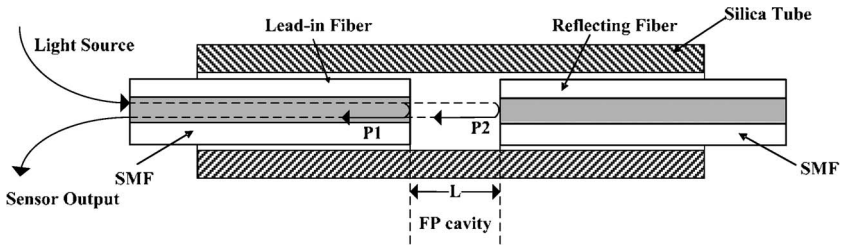

Fig. 1. Schematic diagram of a regular SMF-EFPI sensor.

crack and fracture monitoring in structural health monitoring (SHM). In general, the fringe visibility of an EFPI is determined by the core size, numerical aperture (NA), modal power distribution in the lead-in fiber, and cavity length. One way of improving fringe visibility is to minimize the NA of the lead-in fiber so that the divergence angle of the exiting beam becomes small. Han *et al.* theoretically proved that the fringe visibility of an EFPI with a smaller NA is less sensitive to the change in gap length of the EFPI sensor [9].

To improve the fringe visibility in a long cavity EFPI, Gangopadhyay *et al.* reported an EFPI vibration sensor making use of a coated GRIN lens pigtailed to the lead-in optical fiber [10]. The use of a GRIN lens not only reduced the divergence angle of the beam exiting from the lead-in optical fiber but also increased the area of reception for the light reflected from the second endface. As a result, the initial cavity length was large and the dynamic range of the vibration sensor was extended to 65 μm. However, pigtailing a GRIN lens to an optical fiber requires additional assembly. The use of a GRIN lens also increases the size of the EFPI sensor and decreases the robustness of the device.

A multimode graded index fiber (GIF) guides light in a similar way as a GRIN lens does [11]. Alternatively, a small section of GIF can also function as a collimator if the length of the GIF is a quarter of the period (i.e., a quarter-pitch GIF). GIF-based collimators have been demonstrated useful in various applications such as coupling light between an optical fiber and a MEMS device [12], characterizing the insertion loss and equalizing the output power in optical transmission [13], collecting light in optical biomedical imaging [14], and expanding the beam exiting from a SMF to excite the cladding modes [15]. Because most of GIFs have the same diameter as that of the SMF, they can be easily fusion spliced to a SMF with negligible loss. As such, using a quarter-pitch GIF as the collimator could potentially extend the dynamic range of an EFPI without sacrificing the robustness and increasing the size of the device.

In this paper, a quarter-pitch GIF based collimator is investigated for construction of an EFPI sensor with enhanced fringe visibility and dynamic range. The ray matrix model [16] is employed to find the pitch length of the GIF. The divergence angle of the beam exiting from the GIF-collimated SMF is also experimentally measured as a function of the GIF length and compared with the simulation results. The fringe visibility enhancement of the GIF-collimated EFPI is experimentally studied and compared with that of a regular SMF-EFPI.

2. Principle of Operation

2.1. Fringe Visibility of SMF EFPI

The optical reflection from an uncoated fiber/air interface is small, typically about 4% as a result of Fresnel reflection. The multiple reflections inside a low-finesse Fabry–Perot (FP) cavity can be neglected. As shown in Fig. 1, the uncoated, air-gapped EFPI can be modeled using the following two-beam interference equation [17]:

$$P = P_1 + P_2 + 2\sqrt{P_1 P_2}\cos\left(\frac{4\pi n_0 L}{\lambda} + \varphi_0\right) \quad (1)$$

where P is the optical power of the interference signal; P_1 and P_2 are the powers of the reflected lights from the two endfaces, respectively; φ_0 is the initial phase of the interference signal; L is the cavity length; n_0 is the refractive index of the medium filling the cavity ($n_0 = 1$ for the air-gapped cavity); and λ is the optical wavelength in a vacuum.

The quality of the interference signal is commonly quantified by the fringe visibility (or interference contrast). In general, the higher the fringe visibility is, the larger the SNR and better measurement accuracy. The fringe visibility (V) of an interference signal can be calculated by [18]

$$V = (P_{\max} - P_{\min})/(P_{\max} + P_{\min}) \tag{2}$$

where $P_{\max}$ and $P_{\min}$ are the maximum and minimum powers of the interference signal, respectively. As such, the fringe visibility of the EFPI interference signal given by (1) can be expressed by

$$V = 2\sqrt{P_1 P_2}/(P_1 + P_2) \tag{3}$$

If we further define the ratio of the powers of the two interference beams as

$$k = P_2/P_1, \tag{4}$$

The fringe visibility can also be written as

$$V = \frac{2\sqrt{k}}{1+k} \tag{5}$$

From (4) and (5), the interferometer has a maximum fringe visibility of 1 (or 100%) when the two reflections have an equal power ($P_1 = P_2$ or $k = 1$). However, in most cases, P_2 is smaller than P_1 due to the extra optical losses that the light experiences when propagating through the FP cavity. The optical losses may include reflection from the lead-in fiber endface, the optical absorption of the medium filling the cavity and the recoupling loss into the lead-in fiber. In a typical air-gapped low finesse SMF-EFPI, the dominant loss is caused by the recoupling loss, which increases as a function of the cavity length as a result the beam divergence and misalignment. As such, the fringe visibility decreases as the cavity length increases, setting an up-limit of the cavity length of the sensor.

A number of methods have been investigated to quantify the ratio of P_2 over P_1 and thus the fringe visibility of an EFPI sensor. The most straightforward method is to consider the output light from the SMF as a diverging plane-wave with a uniform cross-sectional intensity distribution as suggested by Murphy *et al.* [19]. Based on this plane-wave model, the ratio k is given by

$$k = \frac{(1-R)^2 a^2}{a + 2L\tan\left[\sin^{-1}(NA)\right]^2} \tag{6}$$

where a is the radius of the core of the SMF fiber, L is the length of the FP cavity, NA is the numerical aperture of the fiber, and R is the reflectivity at the SMF/air interface.

Another method uses Gaussian beam approximation in which the output beam from a cleaved SMF is considered having a cross-sectional intensity distribution of a Gaussian profile [20]. The radial intensity profile of the light at a distance of z from the SMF endface can be approximated as [21]

$$I(r,z) = \frac{2P_0}{\pi w(z)^2}\exp\left(\frac{-2r^2}{w(z)^2}\right) \tag{7}$$

where r is the radial distance from the fiber center, P_0 is the total power of the light, and $w(z)$ is the beam radius at the axial position z, at which the light intensity reduces to $1/e^2$ of its maximum intensity.

The beam radius of the Gaussian beam varies along the propagation direction according to the following equation:

$$w(z) = w_0\sqrt{1 + \left(\frac{Z}{Z_R}\right)^2} \tag{8}$$

in which z_R is the Rayleigh length, which is defined by

$$z_R = \pi w_0^2/\lambda \tag{9}$$

where w_0 is the beam radius at the beam waist where the beam radius is at its minimum. In the case of a SMF, the Gaussian beam waist location is commonly considered at the fiber endface $(z = 0)$ and w_0 is taken as a half of the mode field diameter (MFD) of the fiber. Once the MFD of the SMF is known, the light intensity profile at any location z from the lead-in SMF endface can be calculated.

The incident light is partially reflected at the lead-in fiber endface to provide the first interference component P_1, which can be calculated by integrating the light intensity within the core area of the lead-in fiber, which is given by

$$P_1 = 2\pi R\int_0^a \frac{2P_0}{\pi w_0^2}\exp\left(\frac{-2r^2}{w_0^2}\right)rdr \tag{10}$$

The remaining light enters the FP cavity and propagates through a distance that equals to the cavity length L. It is then partially reflected at the reflecting fiber endface back to the FP cavity. The reflected light travels the same distance L to reach the lead-in SMF endface where it is partially recouped into the fiber. The total power that is coupled into the lead-in fiber is an integration of the Gaussian beam intensity over the reception area of the fiber, which equals the core of the lead-in SMF. As such, the light power recoupled into the lead-in fiber (P_2) is

$$P_2 = 2\pi R(1-R)^2\int_0^a \frac{2P_0}{\pi w_{2L}^2}\exp\left(\frac{-2r^2}{w_{2L}^2}\right)rdr \tag{11}$$

where w_{2L} is the mode field radius at the distance of $z = 2L$, which is given by

$$w_{2L} = w_0\sqrt{1 + (2L/z_R)^2} \tag{12}$$

The ratio k between P_2 and P_1 can thus be written as

$$k = \frac{P_2}{P_1} = (1-R)^2\frac{\int_0^a \frac{1}{w_{2L}^2}\exp\left(\frac{-2r^2}{w_{2L}^2}\right)rdr}{\int_0^a \frac{1}{w_0^2}\exp\left(\frac{-2r^2}{w_0^2}\right)rdr}. \tag{13}$$

Once k is known from (6) or (13), the fringe visibility of the EFPI sensor can be calculated as a function of the cavity length using (5).

2.2. GIF Collimated EFPI

As discussed previously, the fringe visibility of an SMF-EFPI decreases as a function of the cavity length due to the divergence of the beam exiting from a regular SMF, resulting in a limited dynamic range of the sensor. A way to increase the dynamic range is to reduce the beam divergence of the exiting light from the SMF by using a collimator. A GIF is an optical fiber whose core refractive index decreases along its radial direction from the center point. Light travels along the axis of GIF follows an approximately sinusoidal path [22]. The period of this sinusoidal path is defined as the pitch of

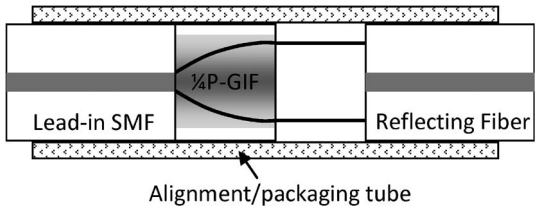

Fig. 2. Schematic illustration of a GIF collimated EFPI.

the fiber. With a SMF feed, by cutting GIF at one quarter of the pitch length, it can serve as a collimating lens.

Here, we study a GIF collimated EFPI sensor as illustrated in Fig. 2, where a quarter-pitch GIF is fusion sliced to the lead-in SMF. The light from the SMF is first collimated by the quarter-pitch GIF before entering the FP cavity. Being a multimode fiber, a GIF also has a large core size and thus a large reception area for the light reflected from the reflecting fiber endface. The light collimation reduces the divergence angle of the beam and the large reception area reduces the coupling loss. Together, they improve the fringe visibility of the EFPI, especially when the FP cavity length is large.

2.3. Ray Matrix Model of the GIF Collimator

The theoretical model of a GIF collimator can be established based on the ray matrix model, which is also known as the ABCD complex beam parameter method, developed by Kogelnik *et al.* [23]. In this model, the light propagation is analyzed as a Gaussian beam. The complex beam parameter $q(z)$ is given by

$$\frac{1}{q(z)} = \frac{1}{R(z)} - i\frac{\lambda}{n\pi w^2(z)} \tag{14}$$

where $q(z)$ is the beam radius at position z, n is the refractive index of the medium that the light is propagating through, $R(z)$ is the radius of curvature of the wavefronts and it evolves along z-direction according to

$$R(z) = z\left[1 + (z_R/z)^2\right] \tag{15}$$

where z_R is the Rayleigh length as defined in Equation (8). At the beam waist location, the radius of curvature becomes infinity and the Gaussian beam has a minimum radius.

The transfer function of q between consecutive planes is given by [24]

$$q_{j+1} = \frac{Aq_j + B}{Cq_j + D} \tag{16}$$

where q_j and q_{j+1} are the complex beam parameters in plane j and plane $j+1$, and the terms A, B, C, and D are the elements of the ray matrix. The system ray matrix is obtained by multiplying the ray matrices of the various optical components that the light propagates through, which is given by

$$\begin{pmatrix} A & B \\ C & D \end{pmatrix} = \prod_{j=0}^{n} M_{j,j+1} \tag{17}$$

where $M_{j,j+1}$ is the ray matrix representation of the optical component between the jth and $(j+1)$th planes.

Fig. 3 shows the ray matrix model schematic of a SMF spliced to a GIF collimator. Planes 1 and 2 are the two sides of the SMF/GIF interface, Planes 3 and 4 are the two sides of the glass/air interface, and Plane 5 is at the Gaussian beam waist of the output beam where the beam width is at a minimum value.

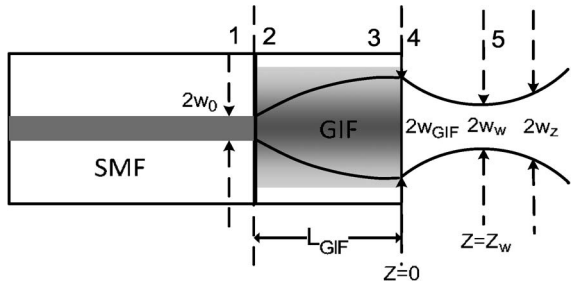

Fig. 3. Schematic of the ray matrix model of the GIF collimator.

To find the Gaussian beam waist of the light exiting from the GIF, we start from the SMF/GIF interface at Plane 1, where the Gaussian beam width is half of the MFD of the SMF. The light propagates through Planes 2 through 4 to reach the Gaussian beam waist location (Plane 5) at a distance $z = z_w$. The ray matrices of the components through which the beam propagates include [22]

$$M_{12} = \begin{pmatrix} 1 & 0 \\ 0 & n_1/n_2 \end{pmatrix} \tag{18}$$

$$M_{23} = \begin{pmatrix} \cos(gL_{GIF}) & \frac{1}{g}\sin(gL_{GIF}) \\ -g\sin(gL_{GIF}) & \cos(gL_{GIF}) \end{pmatrix} \tag{19}$$

$$M_{34} = \begin{pmatrix} 1 & 0 \\ 0 & n_2/n_0 \end{pmatrix} \tag{20}$$

$$M_{45} = \begin{pmatrix} 1 & z_w \\ 0 & 1 \end{pmatrix} \tag{21}$$

where n_1 is the core refractive index of lead-in SMF, n_2 is the core refractive index in the center of the GIF, n_0 is the refractive index of air, z_w is the distance between the GIF/air interface and the Gaussian beam waist location, and g is the focusing parameter defined as

$$g = \sqrt{2\Delta}/b \tag{22}$$

where Δ is the fractional index change at the core-cladding interface, and b is the core radius of the GIF.

Based on (14)–(22), we can find the relative location of beam waist with respect to the lead-in fiber endface (z_w) by setting the radius of curvature $R(z_w)$ equal to infinity in (15), which is given by

$$z_w = \frac{n_0\left[1-(1/z_R n_2 g)^2\right]\sin(gL_{GIF})\cos(gL_{GIF})}{n_2 g\left[\sin^2(gL_{GIF})+(1/z_R n_2 g)^2\cos^2(gL_{GIF})\right]}. \tag{23}$$

We can also find the Gaussian beam waist, which is given by

$$w_w = \frac{w_0}{z_R n_2 g\left[\sin^2(gL_{GIF})+(1/z_R n_2 g)^2\cos^2(gL_{GIF})\right]^{1/2}}. \tag{24}$$

The radius of the Gaussian beam at an arbitrary position z is then

$$w_z = w_w\sqrt{1+\left[\frac{\lambda(z-z_w)}{n_0\pi w_w^2}\right]^2}. \tag{25}$$

The divergence angle of the output beam is approximated as

$$\theta \cong \lambda/(\pi w_w). \tag{26}$$

2.4. Fringe Visibility of the GIF Collimated EFPI

To find the fringe visibility of the GIF collimated EFPI, we first calculate the optical power reflected directly at the GIF fiber endface by integrating the intensity profile over the reception area of the GIF and assume that the coupling coefficient from GIF to SMF of this reflected light is η_1. The reflected light power coupled into the lead-in SMF is

$$P_{1,SMF} = 2\eta_1 \pi R^2 \int_0^b \frac{2P_0}{\pi w_{GIF}^2} \exp\left(\frac{-2r^2}{w_{GIF}^2}\right) rdr \tag{27}$$

where w_{GIF} is the beam radius at the GIF endface, which can be found by setting $z = 0$ in (25), which is given by

$$w_{GIF} = w_w \sqrt{1 + \left[\frac{\lambda(z_w)}{n_0 \pi w_w^2}\right]^2}. \tag{28}$$

To calculate the optical power of the second beam, we first calculate the radius of the Gaussian beam at the distance of $z = 2L$ using (25), which is given by

$$w_{2L,GIF} = w_w \sqrt{1 + \left[\frac{\lambda(2L - z_w)}{n_0 \pi w_w^2}\right]^2}. \tag{29}$$

We assume the coupling coefficient from GIF to SMF for the second beam is η_2. The recoupled power into lead-in SMF through GIF is calculated by integrating the reflected intensity profile at the GIF endface over the core area of the GIF, and then multiplying its coupling efficient η_2, which is given by

$$P_{2,SMF} = 2\eta_2 \pi R(1 - R)^2 \int_0^b \frac{2P_0}{\pi w_{2L,GIF}^2} \exp\left(\frac{-2r^2}{w_{2L,GIF}^2}\right) rdr. \tag{30}$$

The light exiting from the quarter-pitch GIF collimator is close to parallel. Therefore, the coupling coefficients η_1 and η_2 are almost the same and both close to 100%, $\eta_1 \approx \eta_2$. As such, the power ratio of the two reflected lights is

$$k = \frac{P_{2,SMF}}{P_{1,SMF}} = (1 - R)^2 \frac{\int_0^b \frac{1}{w_{2L,GIF}^2} \exp\left(\frac{-2r^2}{w_{2L,GIF}^2}\right) rdr}{\int_0^b \frac{1}{w_{GIF}^2} \exp\left(\frac{-2r^2}{w_{GIF}^2}\right) rdr}. \tag{31}$$

The visibility can thus be obtained using (5) after k is found.

3. Experiment Results and Discussions

3.1. Ray Matrix Simulation of the GIF Collimator

Fig. 4 plots the divergence angle and beam waist of the Gaussian beam as a function of the GIF length based on the ABCD ray matrix model. A commercial GIF (Corning InfiniCor 600) was

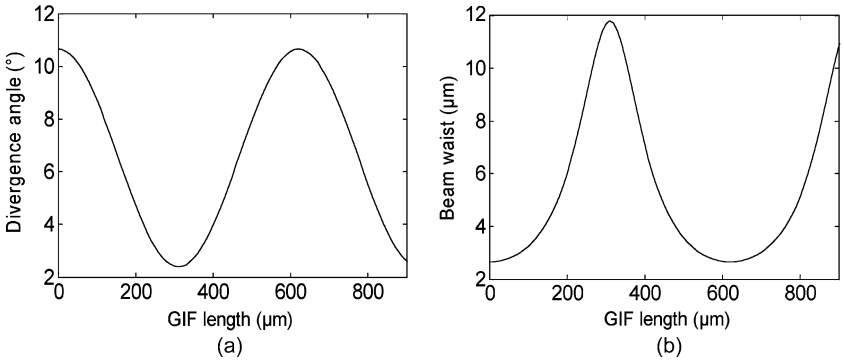

Fig. 4. Simulation result of ray matrix model. (a) Beam divergence angle as a function of the GIF length. (b) Gaussian beam waist as a function of the GIF length.

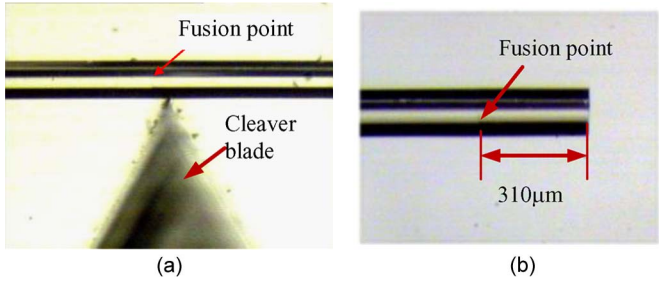

Fig. 5. Microscopic images of GIF collimator (a) Image of the cleaver blade and fused fiber. (b) Image of a cleaved GIF collimator.

employed in the simulations. From the datasheet, it has $\Delta = 1\%$ and a core radius of 25 μm. The simulation results indicate that the first minimum divergence angle occurs when the Gaussian beam waist reaches its maxima at the GIF-air endface. The GIF length at this specific point is one-quarter pitch length. The simulation results predict that the GIF has minimum divergence angle of 2.2° and a quarter pitch length of 320 μm.

3.2. GIF Collimator Fabrication

To fabricate GIF collimators, we first fusion spliced a section of GIF (Corning InfiniCor 600) to a SMF (Corning SMF-28e). The two ends of the spliced fiber were then fixed on two precision translation stages (Newport, PM 40276). By synchronizing the two stages using a programmed stage controller (Newport pm500-c), the spliced fiber was able to move along its axial direction with a resolution of 500 nm. A fiber cleaver (Fujikura High Precision Fiber Cleaver) was placed under the spliced fiber with its blade perpendicular to the fiber axis. By fine tuning the height of the blade, we were able to achieve a good cutting quality.

A microscope was also set up to capture the image of the cleaver blade and spliced fiber as shown in Fig. 5(a). During the cleaving process, we first pre-strained the fiber and moved the translation stages to precisely align the GIF/SMF interface with the cleaver blade. Then, we moved the GIF/SMF interface by a distance of the desired GIF length away from the blade plane. The GIF collimator fabrication was completed by triggering the cleaver blade. To evaluate the accuracy, we also measured the GIF length using a measuring microscope (Nikon Measurescope UM-2). We performed 65 cleaves. The standard deviation of the GIF length was 5.2 μm from the preset values. Fig. 5(b) shows a microscopic image of a fiber collimator with a GIF length of 310 μm.

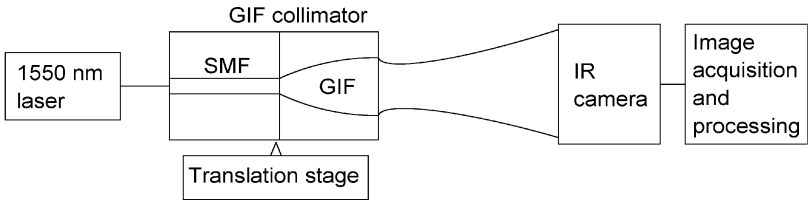

Fig. 6. Schematic of the setup for divergence angle measurement.

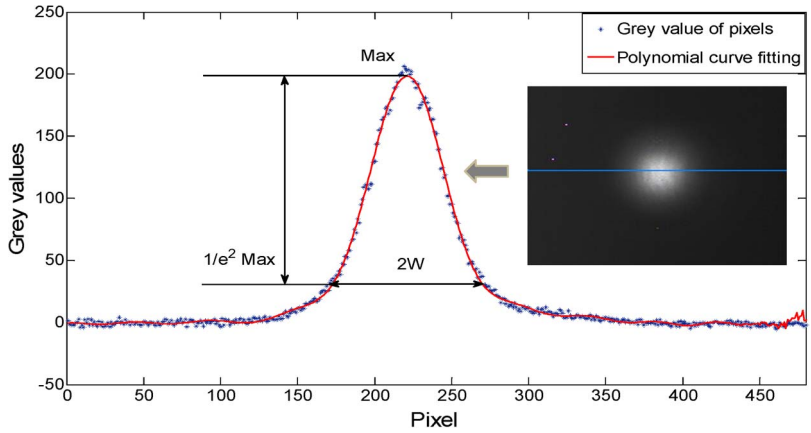

Fig. 7. Far-field intensity distribution of output beam from the GIF collimator. Insert: Far-field IR image obtained by the infrared camera.

3.3. Divergence Angle Measurement

Fig. 6 shows the schematic diagram of the experimental setup to measure the divergence angle of the GIF collimator.

Light from a laser source with a center wavelength of 1550 nm was launched into a SMF spliced with a GIF collimator (310 μm in length). The SMF-GIF collimator was fixed by a fiber holder, which was mounted on a translation stage. An infrared (IR) camera (SU320, Sensors Unlimited Inc.) was installed facing perpendicular to the GIF collimator. We adjusted the stage to ensure that the output beam profile was fully captured by the sensing area of the IR camera. A computer was used to collect the image (640 $\times$ 480 pixels) through a video acquisition card. One pixel of the image corresponded to 12.5 μm in dimension. In order to avoid saturation of the IR camera pixels, the laser power was set to -22 dBm.

The insert of Fig. 7 shows a representative far field IR image obtained by the IR camera. To obtain the beam radius, we drew a horizontal line across the center pixel and plotted the gray level distribution along this horizontal line. As shown in Fig. 7, the gray level followed an approximate Gaussian distribution. A polynomial fit was used to smooth the distribution curve. The two points where their intensity was at the $1/e^2$ of the maximum were then calculated, and the distance between these two points were taken as twice of the Gaussian beam radius.

In the far field, the Gaussian beam width grows linearly as a function of distance from the collimator. The beam radius measured by the camera increases due to beam divergence as the linear translation stage moves the collimator away from the camera. The divergence angle of the output beam can thus be calculated based on the derivative of the Gaussian beam width with respect to the distance that the collimator moves according to the following equation [25]:

$$\theta_{div} = \frac{w(d_2) - w(d_1)}{d_2 - d_1} \tag{32}$$

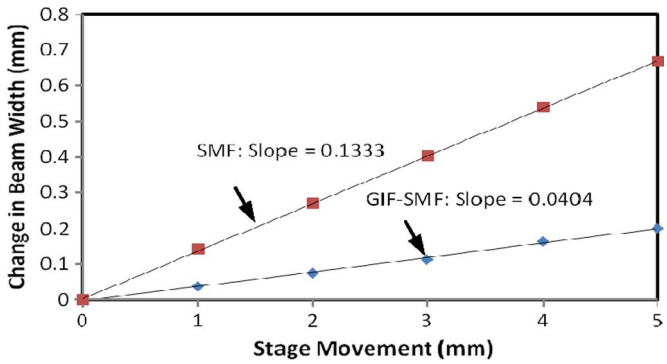

Fig. 8. Changes in Gaussian beam widths as a function of stage movement.

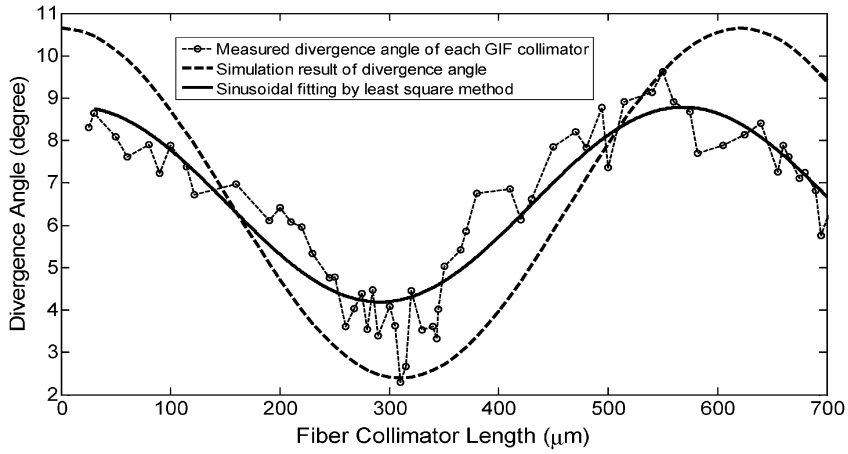

Fig. 9. Divergence angles of the GI F collimator as a function of GIF length.

where $w(d_1)$ and $w(d_2)$ are the Gaussian beam widths at distance d_1 and d_2, respectively. To minimize the error, beam radii were measured at multiple positions. The divergence angle was calculated based on the slope of the linear-fitted line of the beam radius as a function of the fiber positions.

To find the slope, we first recorded the images projected from the GIF collimator at 6 different positions of fiber movements. The distance between two consecutive fiber movements was 1 mm. The beam width of each position was then calculated based on the captured IR image. Fig. 8 shows the far field beam width as a function of the fiber movements using a GIF collimated SMF with the GIF length of 310 μm. The slope of the linear fitted line was found to be 0.0404, corresponding to a divergence angle of 2.3°. To validate the experiment setup and procedures, we also measured the beam divergence angle from a SMF (Corning SMF-28e). Also shown in Fig. 8, the measured slope of the SMF beam was 0.1333. Correspondingly, the divergence angle was 7.7°, which agreed well with the NA (0.14) of the fiber from the datasheet.

Fig. 9 plots the measured divergence angle as a function of the GIF length ranging from 20 μm to 780 μm. The ray matrix simulation result is also shown for comparison. In general, the divergence angle varied as a sinusoidal-like function of the GIF length. We curve fitted the data using a sinusoid function based on the least-square principle for a better visualization. The smallest divergence angle θ was 2.3° measured at the GIF length of 310 μm. The measurement results agreed well with the simulation predictions. In comparison, the measurement results indicated that the divergence angle could be reduced by splicing a GIF collimator with an appropriate length to an SMF.

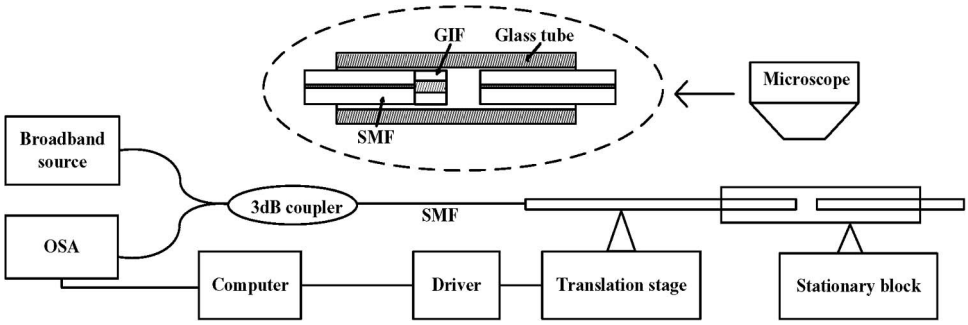

Fig. 10. Schematic illustration of the experiment setup to measure reflected interference signal from the sensor.

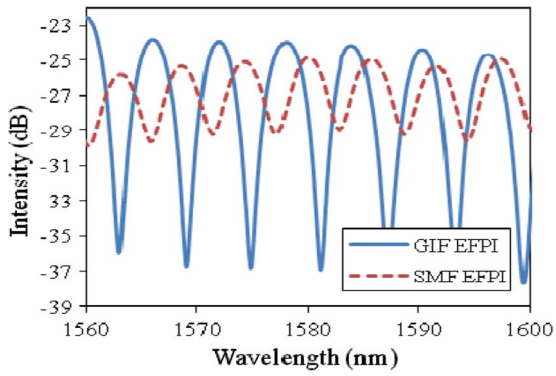

Fig. 11. Interference spectra of the SMF-EFPI and GIF-EFPI at the cavity length of 200 μm.

3.4. Fringe Visibility Measurement

To evaluate the fringe visibility enhancement by using a GIF collimator, both a SMF-EFPI and a GIF-EFPI with different FP cavity lengths were experimentally investigated. A white light interrogation system is set up for fringe visibility measurement as shown in Fig. 10. A broadband source, with a spectrum ranging from 1520 to 1620 nm, was made by multiplexing a C-band (AFC, BBS-1550A-TS) and an L-band (Highwave, HWT-BS-L-P) erbium-doped fiber amplified-spontaneous-emission (ASE) source. The broadband light excited the EFPI device through a 1 $\times$ 2, 3 dB fiber coupler. The reflected interference spectrum from the EFPI was recorded by an optical spectrum analyzer (OSA, AQ6319).

The EFPI was constructed by first inserting a cleaved SMF into a hollow core glass tube with an inner diameter (ID) of 127 μm. Epoxy was carefully applied to bonding the SMF and the glass tube without contaminating the cleaved fiber endface. The glass tube was mounted on a stationary block. A GIF collimated SMF (or a SMF in the case of a regular SMF-EFPI) was then inserted into the tube from the other end of the glass tube. This GIF collimator fiber was mounted on a 3-D precision translation stage through a fiber holder so that it could be moved to change the cavity length. The glass tube ensured the parallelism between fiber endfaces during the movement of the lead-in GIF fiber along its axis. A microscope was also used to assist the assembly process. The actual cavity length was calculated based on the stage movement with a resolution of 500 nm.

In the experiments, we set the initial FP cavity length at 20 μm, and then moved the stage to increase the cavity length. The Interference spectra were recorded at different cavity length until it reached 500 μm. Fig. 11 shows the interference spectrum of a GIF collimated EFPI at the cavity length of 200 μm. The GIF collimator had a length of 310 μm. The interference spectrum of a SMF-EFPI at the same cavity length is also shown for comparison. The fringe contrast of the GIF

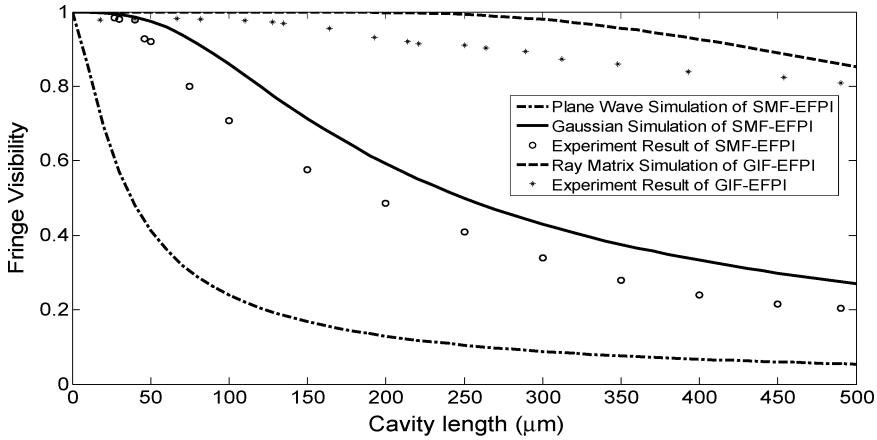

Fig. 12. Fringe visibility comparison between the regular SMF-EFPI and the GIF-EFPI.

collimated EFPI exceeded 13 dB $(V = 0.92)$, while the SMF-EFPI was around 4 dB $(V = 0.43)$, clearly indicating the improvement in fringe visibility by using a GIF collimator.

Fig. 12 plots the measured fringe visibility as a function of the FP cavity length of both SMF-EFPI and GIF-EFPI. The fringe visibilities of both decreased as the cavity length increased, however, the former decreased much faster than the latter. At the cavity length of 500 μm, the fringe visibility dropped to about 0.2 for the SMF-EFPI while that of the GIF-EFPI only dropped to 0.8, which was about the same of a SMF-EFPI with a cavity length of about 80 μm. Simulated fringe visibilities are also plotted in Fig. 12 for reference. The fringe visibility of the SMF-EFPI obtained by the Gaussian model fit the experimental results better than that using the plane wave model. The ray matrix model simulation result of the GIF-EFPI also fit the experiment data in the general trend. However, we did notice that the measured fringe visibilities were constantly smaller than those obtained from simulations. The deviations might be caused by non-ideal factors such as the non-perpendicular cleaving of the fiber and the axial misalignment between the lead-in and reflecting fibers.

The experiment results demonstrated that the fringe visibility of an EFPI could be enhanced by splicing a quarter-pitch GIF onto the lead-in SMF as a collimator, which effectively reduced the divergence angle of the beam traveling inside the FP cavity. The increased fringe visibility could result in a better SNR to improve the measurement accuracy. Besides, a GIF-EFPI could be used at a larger cavity length since its visibility is less sensitive to the increase in cavity length than that of a SMF-EFPI. This could provide a potential solution for large strain measurement in SHM, such as crack opening detection.

4. Conclusion

In this paper, we presented a visibility enhanced EFPI by using a quarter-pitch GIF as a collimator that was fusion spliced to the lead-in SMF. The ABCD ray matrix method was used to model the GIF collimator. The simulation results predicted that a collimator could be obtained by cutting the GIF (Corning InfiniCor 600) at the quarter-pitch length of 320 μm to obtain a minimum divergence angle of 2.2°. GIF collimators were fabricated by controlled fiber cleaving under a microscope with micrometer-level accuracy. The beam divergence angle of a GIF collimated SMF was experimentally measured as a function of the GIF length using an IR camera and image processing at far field. The measurement results were in good agreement with the simulation results. At the GIF length of 310 μm, the measured divergence angle was 2.3°. The fringe visibility as a function of the cavity length was studied theoretically and measured experimentally for both SMF-EFPI and GIF-EFPI. The simulated fringe visibility from Gaussian beam approximation fit better with the measurement results than that using the plane wave model. At the cavity length of 500 μm, the fringe visibility of the GIF-EFPI was 0.8 while that of the SMF-EFPI was only 0.2. We conclude that

the fringe visibility of an EFPI can be effectively enhanced by splicing a quarter-pitch GIF collimator to the lead-in SMF. The visibility enhanced GIF-EFPI provides better a SNR for applications where a large dynamic range is desired such as such as crack opening detection and large strain measurement in structural health monitoring.

References

[1] E. Pinet, "Fabry–Perot fiber-optic sensors for physical parameters measurement in challenging conditions," *J. Sensors*, vol. 2009, pp. 1–9, 2009.

[2] T. Wei, Y. Han, H. L. Tsai, and H. Xiao, "Miniaturized fiber inline Fabry–Perot interferometer fabricated with a femtosecond laser," *Opt. Lett.*, vol. 33, no. 6, pp. 536–538, Mar. 2008.

[3] J. Zhang, G. D. Peng, L. Yuan, and W. Sun, "Composite-cavity-based Fabry–Perot interferometric strain sensors," *Opt. Lett.*, vol. 32, no. 13, pp. 1833–1835, Jul. 2007.

[4] W. Wang, N. Wu, Y. Tian, X. Wang, C. Niezrecki, and J. Chen, "Optical pressure/acoustic sensor with precise Fabry–Perot cavity length control using angle polished fiber," *Opt. Express*, vol. 17, no. 19, pp. 16 613–16 618, Sep. 2009.

[5] J. R. Lawall, "Fabry–Perot metrology for displacements up to 50 mm," *J. Opt. Soc. Amer. A, Opt. Image Sci. Vis.*, vol. 22, no. 12, pp. 2786–2798, Dec. 2005.

[6] P. C. Beard and T. N. Mills, "Extrinsic optical-fiber ultrasound sensor using a thin polymer film as a low-finesse Fabry–Perot interferometer," *Appl. Opt.*, vol. 35, no. 4, pp. 663–675, Feb. 1996.

[7] K. D. Oh, A. Wang, and R. O. Claus, "Fiber-optic extrinsic Fabry–Perot dc magnetic field sensor," *Opt. Lett.*, vol. 29, no. 18, pp. 2115–2117, Sep. 2004.

[8] T. Wei, Y. Han, Y. Li, H. L. Tsai, and H. Xiao, "Temperature-insensitive miniaturized fiber inline Fabry–Perot interferometer for highly sensitive refractive index measurement," *Opt. Express*, vol. 16, no. 8, pp. 5764–5769, Apr. 2008.

[9] M. Han and A. Wang, "Exact analysis of low-finesse multimode fiber extrinsic Fabry–Perot interferometers," *Appl. Opt.*, vol. 43, no. 24, pp. 4659–4666, Aug. 2004.

[10] T. K. Gangopadhyay, "Non-contact vibration measurement based on an extrinsic Fabry–Perot interferometer implemented using arrays of single-mode fibres," *Meas. Sci. Technol.*, vol. 15, no. 5, pp. 911–917, May 2004.

[11] D. V. Baranov, I. V. Zhurilova, S. K. Isaev, L. S. Kornienko, and A. A. Sachkov, "Fiber-optic Fabry–Perot interferometers utilizing graded-index optical waveguides," *Sov. J. Quantum Electron.*, vol. 19, no. 5, pp. 690–692, 1989.

[12] M. Zickar, W. Noell, C. Marxer, and N. de Rooij, "MEMS compatible micro-GRIN lenses for fiber to chip coupling of light," *Opt. Express*, vol. 14, no. 10, pp. 4237–4249, May 2006.

[13] Y. L. Lo, H. C. Chow, and C. Y. Chiang, "Reconfigurable OADM and OXC designed by a new optical switch," *Opt. Fiber Technol.*, vol. 10, no. 2, pp. 187–200, Apr. 2004.

[14] Y. Mao, S. Chang, S. Sherif, and C. Flueraru, "Graded-index fiber lens proposed for ultrasmall probes used in biomedical imaging," *Appl. Opt.*, vol. 46, no. 23, pp. 5887–5894, Aug. 2007.

[15] P. Chanclou, C. Kaczmarek, G. Mouzer, and P. Gravey, "Expanded single-mode fiber using graded index multimode fiber," *Opt. Eng.*, vol. 43, no. 7, pp. 1634–1642, Jul. 2004.

[16] S. Gangopadhyay and S. Sarkar, "ABCD matrix for reflection and refraction of Gaussian light beams at surfaces of hyperboloid of revolution and efficiency computation for laser diode to single-mode fiber coupling by way of a hyperbolic lens on the fiber tip," *Appl. Opt.*, vol. 36, no. 33, pp. 8582–8586, Nov. 1997.

[17] B. Qi, G. R. Pickrell, J. Xu, P. Zhang, Y. Duan, W. Peng, Z. Huang, W. Huo, H. Xiao, R. G. May, and A. Wang, "Novel data processing techniques for dispersive white light interferometer," *Opt. Eng.*, vol. 42, no. 11, pp. 3165–3171, Nov. 2003.

[18] Z. Y. Huang, "Quasi-distributed intrinsic Fabry–Perot interferometric fiber sensor for temperature and strain sensing," Ph.D. dissertation, Virginia Polytechnic Inst. State Univ., Blacksburg, VA, 2006.

[19] K. A. Murphy, M. F. Gunther, A. M. Vengsarkar, and R. O. Claus, "Quadrature phase-shifted, extrinsic Fabry–Perot optical fiber sensors," *Opt. Lett.*, vol. 16, no. 4, pp. 273–275, Feb. 1991.

[20] V. Arya, M. de Vries, K. A. Murphy, A. Wang, and R. O. Claus, "Exact analysis of the extrinsic Fabry–Perot interferometric optical fiber sensor using Kirchhoff's diffraction formalism," *Opt. Fiber Technol.*, vol. 1, no. 4, pp. 380–384, Oct. 1995.

[21] H. Huang and U. Tata, "Simulation, implementation, and analysis of an optical fiber bundle distance sensor with single mode illumination," *Appl. Opt.*, vol. 47, no. 9, pp. 1302–1309, Mar. 2008.

[22] C. Jack and W. Emkey, "Analysis and evaluation of graded-index fiber-lenses," *J. Lightw. Technol.*, vol. LT-5, no. 9, pp. 1156–1164, Sep. 1987.

[23] H. Kogelnik, "On the propagation of Gaussian beams of light through lenslike media including those with a loss or gain variation," *Appl. Opt.*, vol. 4, no. 12, pp. 1562–1569, Dec. 1965.

[24] R. Kishimoto and M. Koyama, "Coupling characteristics between single-mode fiber and square law medium," *IEEE Trans. Microw. Theory Tech.*, vol. MTT-30, no. 6, pp. 882–893, Jun. 1982.

[25] Y. C. Lin, S. C. Lin, and R. H. Wang, "A simplified method for measuring the MFD of single mode fiber using beam scanner," presented at the Electron Devices Materials Symposia, Kaohsiung, Taiwan, 2005, Paper DP14.